Journal of Materials Chemistry A

Accepted Manuscript

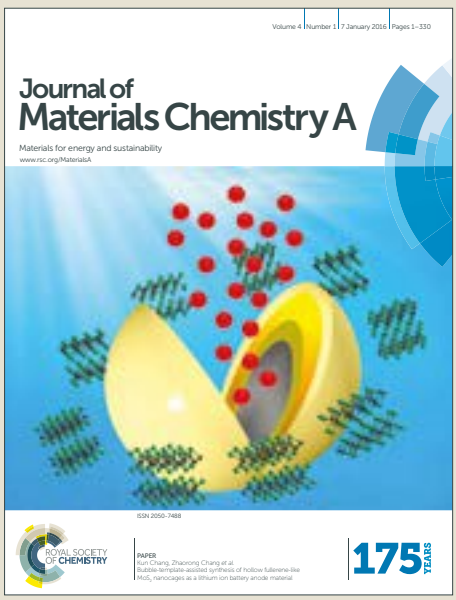

ROYAL SOCIETY OF CHEMISTRY

rsc.li/materials-a

View Article Online
DOI: 10.1039/C7TA06578G

Atmospheric pressure chemical vapor deposition of methylammonium bismuth iodide thin films

Xiao Chen[1], Yoon Myung[1,2], Arashdeep Thind[3], Zhengning Gao[3], Bo Yin[3], Meikun Shen[4], Sung Beom Cho[1], Peifu Cheng[1], Bryce Sadtler[3,4], Rohan Mishra[1,3], Parag Banerjee[1,3,]*

[1]Department of Mechanical Engineering and Materials Science, Washington University in St. Louis, St. Louis, MO – 63130, USA

[2]Department of Nanotechnology and Advanced Materials Engineering, Sejong University, Seoul, 05006, Korea

[3]Institute of Materials Science & Engineering, Washington University in St. Louis, St. Louis, MO – 63130, USA

[4]Department of Chemistry, Washington University in St. Louis, St. Louis, MO – 63130, USA

*Email - parag.banerjee@wustl.edu

Keywords: Methylammonium bismuth iodide, chemical vapor deposition (CVD), Hall measurements, lead-free photovoltaics

Abstract:

We demonstrate the atmospheric pressure chemical vapor deposition of methyl ammonium bismuth iodide ($(CH_3NH_3)_3Bi_2I_9$ or $MA_3Bi_2I_9$) films. $MA_3Bi_2I_9$ possesses an indirect optical bandgap of 1.80 eV and a room temperature excitonic peak at 511 nm. In contrast to recent reports, the films are *n*-type semiconductors with a room temperature carrier concentration of 3.36×10^{18} cm^{-3} and Hall mobility of 18 $cm^2/V.s$; values superior to solution-processed, undoped

View Article Online
DOI: 10.1039/C7TA06578G

films. The precursors used for the deposition are methylammonium iodide and bismuth iodide which are co-sublimated at 199 ^{o}C and 230 ^{o}C, respectively in Ar flow inside a tube furnace with a variable temperature profile. The substrate temperature is set at 160 ^{o}C, and dense polycrystalline films ~ 775 nm thick are deposited. Extensive characterization combined with first-principles density functional theory calculations unravel the synthesis-structure-property relationship in these films. Degradation of properties in ambient results from film oxidation with a characteristic bi-exponential decay in resistivity, signifying a fast surface oxidation followed by a slower oxidation of the bulk.

1 Introduction

Lead halide perovskites ($CH_3NH_3PbI_3$ or $MAPbI_3$ and its variants) are promising solar-cell absorber materials with reported power conversion efficiencies that have rapidly increased from[1] 3.8% in 2009, to an impressive[2] 22.1% in 2017. The fundamental material properties in lead halide perovskites that drive such progress are its high charge-carrier mobilities[3], high optical absorption coefficient,[4] ideal and tunable bandgap[5] and ultra-long carrier diffusion lengths up to a few microns.[3, 6, 7]

Though the reported power conversion efficiencies of lead halide perovskite solar cells are now competitive with commercial silicon solar cells, there are two limitations preventing the commercialization of such solar cells.[8] These are (1) the environmental, device and thermodynamic instability[9, 10] of the perovskites in the presence of air, humidity, light and electric fields; and (2), the toxicity[11] due to the presence of lead. Attempts to address stability limitations have included replacing the A-site organic component ($CH_3NH_3^+$) with inorganic cations[12, 13], such as Cs^+ and Rb^+ or by providing protective overlayers[14] that prevent exposure of

View Article Online
DOI: 10.1039/C7TA06578G

lead halide perovskite films to ambient conditions. However, the toxicity due to the presence of lead in these perovskites presents a challenge to further scale-up and eventual commercialization. Recently, bismuth[15-17] (Bi^{3+}) has drawn attention[18] as a substituent to the B-site occupied by Pb^{2+} for 'lead-free' perovskites,[19] since it is a non-toxic 6p-block element that is isoelectronic[20, 21 22] with Pb^{2+}. Reports on promising optoelectronic and photovoltaic properties of methylammonium bismuth iodide (with formula unit $(CH_3NH_3)_3Bi_2I_9$ and henceforth called $MA_3Bi_2I_9$) with high absorption coefficient[23] and long term stability[24] have been published. However, $MA_3Bi_2I_9$ based solar cells suffer from low efficiency.[25] Besides the sub-optimal electronic structure of $MA_3Bi_2I_9$ compared to $MAPbI_3$,[17 26] the diminished performance of the solar-cells is also attributed to the commonly used solution deposition techniques that result in poor morphology, purity and coverage of the films on substrate. [27, 28]

Thus in this Article, we demonstrate a gas-phase deposition technique for $MA_3Bi_2I_9$ thin films using a low temperature (160 ^oC), atmospheric pressure chemical vapor deposition (APCVD) process. We obtain films with better control over morphology, purity and coverage with the added advantage of rapid scale-up and integration with other solar manufacturing processes. The APCVD process occurs in a tube furnace by taking advantage of the variable temperature gradient along the length of the tube. Specific temperature zones within the tube are utilized to co-sublimate methylammonium iodide (with chemical formula unit CH_3NH_3I and referred henceforth as MAI) and bismuth iodide (BiI_3) into vapor form, which condenses and reacts on the cooler, downstream side of the tube furnace. The result is an *n*-type, dense and polycrystalline $MA_3Bi_2I_9$ film with an optical bandgap of 2.08 eV, a room-temperature free electron carrier density of 3.36 x 10^{18} cm^{-3} and Hall mobility of 18 $cm^2/V.s$. We discuss the

View Article Online
DOI: 10.1039/C7TA06578G

synthesis-structure-property interrelationship in $MA_3Bi_2I_9$ films obtained from a suite of characterization techniques and first-principles density functional theory (DFT) calculations.

2 Experiment

2.1 Methylammonium iodide preparation

Methylammonium iodide (MAI) was synthesized using minor modifications to a previously published procedure[29]. First, 25 mL of methylamine (33 wt% in ethanol, Sigma-Aldrich) was added to a 250 mL, three-neck flask maintained at a temperature lower than 7°C. 10 mL of hydroiodic acid (HI, 57 wt% in water, Sigma-Aldrich) was added dropwise to the flask at a speed of approximately 6 drops/10secs to MAI solution while the solution was stirred at 300 rpm. The white MAI precipitate was recovered from the solution using rotary evaporation at a pressure of 60 Torr with the flask in a water bath at 50 °C.

The collected MAI powder was dissolved in 10 ml absolute ethanol while stirring and sonicating for 10 minutes and then precipitated by adding 50-55 ml of diethyl ether to the solution and refrigerating it for 20 minutes. After filtration, the process was repeated 3 times, and finally a white powder was obtained and dried at 60 °C overnight under vacuum using a Schlenk line. The phase purity of the compound was confirmed by a Bruker D8 Advance powder X-ray diffractometer (**supporting information S1**).

2.2 Perovskite synthesis via APCVD

The MAI powder prepared above was used as a first precursor for the APCVD. BiI_3 powder (99%, Aldrich) was used as a second precursor for the APCVD and used without further purification. A quartz tube mounted on a single zone furnace (Compact Split Tube Furnace with 1" Tube-OTF-1200X-S, MTI Corporation.) was used for all APCVD studies. Silicon wafers (Test Grade, University Wafers Inc.) with or without a 100 nm thermal oxide layer, glass slides

View Article Online
DOI: 10.1039/C7TA06578G

(48300-025, VWR), pre-cut 5 mm x 5 mm high purity quartz substrates (MTI Corporation) and 2 cm x 2 cm Willow® flexible glass from Corning were used as substrates. The silicon and glass substrates were cut to approximately 1 cm x 2 cm size, ultrasonically cleaned in DI water, acetone (99.9% Aldrich) and ethanol (99.9% Aldrich) mixture for 10 minutes, washed by IPA and DI water, dried in compressed air, cleaned in UV Ozone (Ossila E511) for 10 minutes, and then immediately placed in the quartz tube, 23 cm away from the upstream end.

The schematic of the experimental set-up is shown in **Figure 1a**, while a picture of the furnace after successful $MA_3Bi_2I_9$ deposition is shown in **Figure 1b**. The deposition is marked by the characteristic orange color of the $MA_3Bi_2I_9$ film on the downstream side.[15] Initially, 50 mg of MAI and 60 mg of BiI_3 were used as sources and placed at 2.5 cm and 13 cm from the upstream end of the quartz tube in alumina boat crucibles. First, the quartz tube was purged with 280 standard cubic centimeters per minute (sccm) flow of ultra-high purity Ar gas (UHP 300, Airgas) for 10 minutes. The temperature in the quartz tube was then raised at the rate of 1.8 ^{o}C / minute until the temperature at the center of the tube reached 230 ^{o}C. The furnace was maintained at this temperature for various times of 15, 30, 45, 60, 90, 180, 240, 360 and 480 minutes of deposition. After deposition, the furnace was naturally allowed to cool down to ambient temperature. This usually took 3 hours.

The key aspect of an APCVD process lies in the precise placement of the MAI and BiI_3 sources along the length of the quartz furnace reactor. This allows us to co-sublimate both the sources together. **Figure 1c** shows the temperature profile of the furnace along the length of the CVD quartz tube. This calibration measurement was done prior to the deposition by sliding a thermocouple probe inserted inside the quartz tube with Ar flowing at the rate of 280 sccm. The temperature varies from 199 ^{o}C from the upstream end (labeled as 2.5 cm on the x-axis) and

View Article Online
DOI: 10.1039/C7TA06578G

peaks to the desired temperature set-point of the furnace (230 ^{o}C) at the center of the tube (13 cm from the upstream end). The temperature then drops off on the downstream side to 160 ^{o}C, 23 cm from the upstream end.

The variability of the temperature along the length of the quartz furnace reactor is exploited in the APCVD process. The MAI boat is placed at 2.5 cm from the upstream side where the temperature is 199 ^{o}C and allows the MAI to sublimate. We note that MAI has a melting point of 270 ^{o}C. The BiI_3 is kept in the middle of the quartz reactor where the temperature is 230 ^{o}C. BiI_3 has a melting point[30] of 402 ^{o}C but is known to sublimate as well. Thus, the Ar flow causes the simultaneous transport of MAI and BiI_3 vapor to the cooler zone in the downstream region. Condensation and reaction of the MAI and BiI_3 vapors take place to produce the $MA_3Bi_2I_9$ film at around 23 cm from the upstream side, where the temperature is maintained at 160 ^{o}C.

Thermogravimetric measurements have been used to calculate vapor pressure of the two precursors, MAI and BiI_3. The details of this analysis are provided in **supporting information S2**. The enthalpy of sublimation of MAI is obtained from Dualeh et al.,[31] to be 105 ± 5 kJ/mol, and for BiI_3 is estimated in this work to be 128 ± 2 kJ/mol. The sublimation temperatures at atmospheric pressure for MAI and BiI_3 are found to be 247 ± 26 ^{o}C and 316 ± 2 ^{o}C, respectively. Based on this analysis, the partial pressure of MAI and BiI_3 when the total pressure is 760 Torr, at the points of sublimation and deposition has been calculated. The vapor pressure as a function of temperature is provided in **Table 1**. At the points of sublimation (199 ^{o}C for MAI and 230 ^{o}C for BiI_3), it can be seen that the partial pressure of MAI is higher than BiI_3 by 4.7x. As the vapor moves downstream, the temperature drops and at 160 ^{o}C (i.e., the deposition temperature), the MAI vapor pressure is 87x higher than BiI_3. Further the thermodynamic driving force for

View Article Online
DOI: 10.1039/C7TA06578G

condensation which is given as,[32] $\Delta G|_{gas \rightarrow solid} = -(\Delta H_{sub}) \times \frac{(T_{sub} - T)}{T_{sub}}$ is found to -17.57 kJ/mol for MAI but -33.9 kJ/mol for BiI_3 using data from **supporting information S2**. This implies that the BiI_3 should readily condense on the substrate, nucleate and grow. On the other hand, MAI condensation followed by a solid-state reaction with BiI_3 to form $MA_3Bi_2I_9$ may be a kinetically rate determining step for $MA_3Bi_2I_9$ film formation. Evidence to this effect will be presented and discussed in the Results & Discussion section.

2.3 Film characterization

Film morphology was characterized by a JEOL JSM-7001 LVF Field Emission SEM under an accelerating voltage of 10 kV. X-ray diffraction (2θ scans) of deposited $MA_3Bi_2I_9$ films were obtained by Rigaku IV X-ray diffractometer using the Cu Kα X-ray source (λ = 1.5405 Å) within a diffraction angle (2θ) from 5° to 60°. X-ray photoelectron spectroscopy (XPS) was measured using the PHI Versa Probe II spectrometer (Physical Electronics) with a photon energy of 1486.6 eV (Al Kα). The absorption spectrum of a $MA_3Bi_2I_9$ film deposited onto an ITO substrate was measured using a Perkin-Elmer Lambda 950 spectrometer equipped with a 150 mm integrating sphere, a PMT detector, a tungsten halogen lamp for the visible region (350–800 nm), and a deuterium lamp for the ultraviolet region (250–350 nm). The scan rate for the measurement was 0.4 nm/s, and the data interval was 1.0 nm. The film was placed in the center of the integrating sphere to collect both the transmitted, T, and the reflected, R, (including the spectrally reflected and diffusely scattered) light with the PMT detector. The transflectance measurement allowed for the absorbance, A, of the film to be determined by $A = -\log(T + R)$.

The electrochemical analysis was performed with a standard three-electrode cell using the cyclic voltammetry (CV) mode in a Biologic potentiostat (SP-200, Bio-Logic SAS) with a scan rate of 20 mV/s. A glassy carbon electrode was used as the working electrode to measure

View Article Online
DOI: 10.1039/C7TA06578G

the formal potential of ferrocene/ferrocenium (Fc/Fc^+), whereas the Pt foil acted as the counter electrode. Silver (Ag) wire in 0.01 M $AgNO_3$ + 0.1 M tetrabutylammonium hexafluorophosphate ($TBAPF_6$) (98%, Aldrich) in acetonitrile (99.9%, Sigma-Aldrich) was used as the reference electrode (BAS Inc.). The conduction band (CB) energy was calculated from the onset of reduction potential (E_{red}) values, assuming the energy level of Fc/Fc^+ to be −4.8 eV below the vacuum level. The formal potential of Fc/Fc^+ was measured to be 0.075 V against a Ag/Ag^+ reference electrode in an electrolyte consisting of 0.001 M ferrocene in 15 mL of 0.1 M $TBAPF_6$ in acetonitrile solution . Therefore, from equation (1)

$$E_{CB}\ (E_{LUMO}) = -\ (E_{red} + 4.725)\ \text{eV}, \qquad [1]$$

where, the onset potential values (E_{red}) are relative to the Ag/Ag^+ reference electrode. The valence band (VB) energy, E_{VB} (E_{HOMO}) was calculated based on the band gap value determined from UV−vis spectra, E_{VB} (E_{HOMO}) = E_{CB} −E_g (indirect). $MA_3Bi_2I_9$ films deposited on glass slides were dissolved in a solution of 0.1 M tetrabutylammonium hexafluorophosphate ($TBAPF_6$), acetonitrile for conducting these tests.

All electronic transport property measurements were carried out in a commercial probe station (Janis ST500-1-2CX) with Cu–Be probe tips having 50 μm tip diameter. A Keithley 2400 source meter was used for resistivity measurements on $MA_3Bi_2I_9$ films deposited on 5 mm × 5 mm high-purity quartz substrates (MTI Corp). Van der Pauw structures were created by first sputtering 50 nm Pt on the four corners of the quartz substrates prior to $MA_3Bi_2I_9$ deposition. After $MA_3Bi_2I_9$ deposition, indium dots were attached to these four corners and served as the contact electrodes for the four probe tips. Corresponding Hall measurements were done by placing an Fe-Nd ring magnet around the sample. The magnetic field strength at the center of the ring magnet was 2135 G. The pressure in the chamber was maintained at or below $1x10^{-4}$ Torr.

View Article Online
DOI: 10.1039/C7TA06578G

2.4 DFT calculation details

DFT calculations were performed using the Vienna Ab-initio Simulation Package (VASP).[33] We employed the Perdew-Burke-Ernzerhof exchange-correlation (XC) functional revised for solids (PBEsol).[34] The core and valence electrons were modeled using the projector-augmented-wave (PAW) method.[35] We used a plane-wave basis set with a cutoff of 500 eV and performed relaxation until the Hellmann–Feynman forces on the atoms were less than 0.001 eV/Å. The Brillouin zone was sampled using a Gamma-centered Monkhorst-Pack[36] *k*-points mesh while keeping the *k*-points density ($n_k \times a$), where n_k is the number of *k*-points and *a* is the lattice parameter, equal to ~26 for structural relaxation and ~52 for electronic structure calculations. The spin-orbit coupling (SOC) effects were included for calculating the electronic band structure and the absorption spectra. The charge partitioning for the Bader charge analysis was carried out using the approach developed by Henkelman et al.[37-39] The elemental charges, used for Bader charge analysis, are the difference between the total valence electrons considered in the PAW potential and the total electrons assigned to an element after the charge density partitioning. The band-edge alignment for $MA_3Bi_2I_9$ was performed using a surface slab with material thickness of ~55 Å and a vacuum of ~50 Å. The valence band edge (E_{VB}) is calculated using the expression, $E_{VB} = \phi_{VAC} - \varepsilon_{VB}$, where Φ_{VAC} is the vacuum electrostatic potential and ε_{VB} is the eigenvalue for the valence band maxima. The conduction band edge (E_{CB}) is calculated using the expression, $E_{CB} = E_{VB} + E_G$, where E_G is the band gap calculated using PBEsol with SOC.

View Article Online
DOI: 10.1039/C7TA06578G

3 Results & Discussion

3.1 Materials characterization

Figure 2a shows the color of the films on glass substrates as a function of deposition time. Initially, for short times (< 60 minutes), there is hardly any deposition observed. After 90 minutes of reaction, a visible orange color is seen on the glass substrate. We note that there is a stronger color close to the upstream side of the sample, indicating that the deposition is determined by the Ar flow. For films ≥ 180 minutes, a continuous film is observed on the glass substrate. The orange color is characteristic of $MA_3Bi_2I_9$.[15] Successfully deposition of $MA_3Bi_2I_9$ films on Willow® glass - Corning's flexible glass substrate is shown in **Figure 2b** and **Figure 2c**. These flexible glass substrates can withstand temperatures up to 500 ^oC and thus, can be used for the APCVD of $MA_3Bi_2I_9$ films.

High-magnification SEM images are shown for the same substrates in **Figure 3**. Mechanistic aspects of the deposition process can be garnered from this sequence of images. First, **Figure 3a, b** and **c** (i.e., for deposition times 15, 30 and 45 minutes) show isolated hexagonal crystals growing in size from 0.5 μm for 15 minutes, to 1.0 μm for 45 minutes of deposition. The crystal shape is characteristic of BiI_3[40] and has been independently confirmed by through Raman (see **supporting information S3**) and XRD measurements, as will be shown below. Thus, in the initial part of the deposition scheme, isolated BiI_3 crystals 0.5 – 1.0 μm in diameter are deposited on the substrate surface.

The BiI_3 crystals show signs of MAI incorporation starting at 60 minutes (**Figure 3d**). While the crystal shapes remain intact, the surface of the crystal shows marked roughness. For 90 minutes (**Figure 3e**), the deposited structure becomes interconnected. The interconnected

View Article Online
DOI: 10.1039/C7TA06578G

structure shows signs of growth for 180 minutes (**Figure 3f**) while the surface structure is rough and full of pinholes.

The surface structure further changes for the 240-minute sample (**Figure 3g**), where well-crystallized $MA_3Bi_2I_9$ grains are visible, though evidence of MAI incorporation can still be seen at the grain boundaries. For the 360-minute sample (**Figure 3h**), the $MA_3Bi_2I_9$ polycrystalline grains are well developed, indicating complete incorporation of the MAI. However, there are intergranular gaps observed, and such morphology is not ideal for thin film photovoltaic application. Finally, for the 480-minute sample (**Figure 3i**), we see secondary nucleation of grains in between larger polycrystalline grains.

The secondary nucleation of the $MA_3Bi_2I_9$ crystals observed in the intergranular regions of the film has been used to grow a dense, compact and polycrystalline film. In **Figure 4a** a low-magnification image of the 360-minute sample is shown. The intergranular regions are clearly observed and, as indicated before, are sites for secondary nucleation after 480 minutes of deposition. Therefore, repeating the process twice (labeled henceforth as, 360 minute (2x)), can eliminate these gaps and produce a film with dense morphology. This is shown in **Figure 4b**. While such an approach may see excessive long deposition times, its need is dictated primarily by the limited mass loading of the MAI and BiI_3 precursors in our sublimation crucibles. Larger furnace reactors may easily overcome such hardware limitations and yield dense films in a single process run. The 'twice deposited' films were subsequently used to conduct all optical and electrical measurements.

XRD data of $MA_3Bi_2I_9$ samples deposited for times varying from 15 minutes to 60 minutes are shown in **Figure 5a**. Initially a diffraction peak corresponding to single crystal BiI_3 with violet symbol '■' can be seen. The peak at $2\theta = 52.9°$ can be indexed[41] to BiI_3 (0012). The

View Article Online
DOI: 10.1039/C7TA06578G

other peaks represent MAI, marked by the red symbol '●', (JCPDS ref no. 000-10-0737) at 54.6° corresponding to (222), and a slightly displaced peak from polycrystalline BiI_3 (JCPDS 48-1795) given as '□' at 56.2° corresponding to (226). As deposition time increases, it can be seen that the presence of MAI (JCPDS 10-0737) becomes prominent and the single crystal and polycrystalline BiI_3 signal diminishes.

Figure 5b shows the XRD for deposition times varying from 90 minutes to 480 minutes. After 90 minutes' of deposition, the presence of $MA_3Bi_2I_9$ is detectable. The $MA_3Bi_2I_9$ phase is denoted by the cyan '♦' symbol. Here, we note that there are no JCPDS files available for $MA_3Bi_2I_9$, and we use the patterns generated by Abulikemu et al.,[42] to index our peaks. Initially at 90 minutes, peaks at 29.07° (024), 31.6° (025), 32.38° (116) and 44.7° (029) are observed. A strong peak at 24.6° corresponds to MAI (110). Though unlikely at this early stage of deposition, this peak could also represent the $MA_3Bi_2I_9$ (006) peak at 24.5°. At 180 minutes, the primary peak is still assigned to MAI (110) at 24.6°. Beyond 180 minutes, multiple peaks of $MA_3Bi_2I_9$ start to emerge. The peak at 24.6° can be now assigned to $MA_3Bi_2I_9$ (006), given that there are associated peaks, all corresponding to $MA_3Bi_2I_9$ phase emerge. Other strong peaks corresponding to $MA_3Bi_2I_9$ observed are at 23.6° (015), 25.3° (022), 32.2° (116), 41.07° (028), 44.7° (029) and 50.1° (136). The characteristically polycrystalline nature of the $MA_3Bi_2I_9$ films is in-line with SEM data since polycrystallinity is clearly shown in SEM images for 240-, 360- and 480-minute samples. Finally, we note that there appears to be a weak peak observed for the 240 minute sample at 35.2° corresponding to (116) plane in polycrystalline BiI_3 which could indicate concurrent deposition of BiI_3 during $MA_3Bi_2I_9$ formation, but this peak is not detected for the 360 and 480 minute samples.

View Article Online
DOI: 10.1039/C7TA06578G

Next, we compare the lattice parameters from our XRD results to the crystal structure data obtained from first-principles DFT calculations. $MA_3Bi_2I_9$ exhibits hexagonal crystal symmetry at room temperature with $P6_3/mmc$ space group.[43-45] The methylammonium cation ($CH_3NH_3^+$ (MA^+)) shows no preferential ordering in the hexagonal phase.[43] **Figure 5c** shows the DFT-optimized crystal structure of $MA_3Bi_2I_9$ oriented along [100] and [001] directions. The geometry optimization has been performed using the PBEsol functional,[34] which gives good agreement of theoretical lattice parameters with the experimental values. The calculated lattice parameters from DFT are 8.72 Å, 8.27 Å and 21.76 Å, which are, respectively, within 1.77%, 3.47% and 0.01% of the experimental[43] lattice parameters of the hexagonal phase. Since, we use a static ground-state orientation of the MA cation in our DFT calculations, the ideal hexagonal $P6_3/mmc$ symmetry of the lattice is broken, which results in lowering of the symmetry for the relaxed structure. Instead the DFT relaxed structure exhibits a monoclinic symmetry with space group symmetry Cc, which is a subgroup of $P6_3/mmc$.

The $MA_3Bi_2I_9$ structure can be thought of as a derivative of the perovskite (ABX_3) structure. In both cases the *B*-site cation (Bi in case of $MA_3Bi_2I_9$) is octahedrally coordinated by *X*-site anions (I in case of $MA_3Bi_2I_9$). However, as compared to the ideal perovskite structure, only 2/3rd of the total octahedral sites are occupied by the Bi cation in $A_3Bi_2I_9$ compounds.[16] Additionally, as opposed to the corner-connected octahedral network of BX_6 octahedra in perovskites, $MA_3Bi_2I_9$ forms a layered structure consisting of isolated $Bi_2I_9^{3-}$ bioctahedra. These bioctahedra are formed by two face-shared BiI_6 octahedra, which share three I anions **Figure 5c**).

Figure 6 shows the XPS fine spectra of the 15-, 180- and 480-minute $MA_3Bi_2I_9$ films whereas the full survey spectra of these samples are provided in **supporting information S4**. In **Figure 6a**, the C 1s fine spectrum is shown. For the 15-minute sample, the primary peak is at

View Article Online
DOI: 10.1039/C7TA06578G

284.5 eV corresponding to the C-C bond related to adventitious carbon. There is a slight shoulder detected at 282.6 eV, which is related to the C-N bond[46] originating from MAI. The C-N bond increases in strength for the 180-minute sample and dominates the C 1s signal for the 480-minute sample. These data suggest that MAI incorporation in the BiI_3 is a slower process than the BiI_3 condensation, nucleation and growth process. This conclusion is in line with earlier observations made from vapor pressure calculations in **Table 1** as well as SEM images in **Figure 3**.

N 1s, Bi 4f and I 3d XPS fine spectra are provided in **Figure 6b, c** and **d**, respectively and the peak positions are shown in **Table 2**. For the N 1s, the 15-minute sample shows a weak signal but progressively grows stronger for the 180- and 480-minute samples indicating MA^+ incorporation. The N 1s peak position shifts to lower binding energy from 402.0 eV to 401.5 eV. The Bi 4f and I 3d peaks are strong even at 15 minutes and indicate the presence of BiI_3. MA^+ incorporation produces a shift to lower binding energy of 0.7 eV and 0.5 eV in the Bi 4f and I 3d peaks, respectively. The peak-shifts indicate electron transfer to the N, Bi and I during the transformation of BiI_3 to $MA_3Bi_2I_9$.

To explain the shifts in the XPS spectra, Bader charge analysis has been performed for each element during the chemical reaction leading up to the formation of $MA_3Bi_2I_9$. The average Bader charges for each elemental species in $MA_3Bi_2I_9$, MAI and BiI_3 are shown in **Table 3**. Recall that in **Figure 6a**, the intensity of the de-convoluted C-N peak increases as the reaction proceeds, indicating increased presence of C-N bond with increasing reaction time. The C-N bond occurs at a higher binding energy compared to the C-C bond, signifying loss of electrons in the C atom upon N addition. From the Bader analysis, one finds loss of electrons on the C atom confirmed by the higher atomic charge on C in $MA_3Bi_2I_9$ $(+0.453 \pm 0.015)e$ than in MAI

View Article Online
DOI: 10.1039/C7TA06578G

(+0.445*e*). However, for N there is disagreement between the calculated charge transfer and the shift in XPS peak presented in **Figure 6b**. According to calculated Bader charges, the average charge on N is (–2.982 ± 0.009)*e* and (–3.029*e*) for $MA_3Bi_2I_9$ and MAI respectively, which means N anion is being oxidized while going from MAI to $MA_3Bi_2I_9$. However, this charge transfer is not supported by the shift in the XPS peak towards lower binding energy with increasing reaction time, which points towards the reduction (gain in electrons) of N anion. This disagreement could be attributed to the weak XPS intensity for N at reaction times of 15 and 180 minutes, which makes the determination of charge transfer difficult with the N 1s fine spectra.

The Bi cations in $MA_3Bi_2I_9$ have an average charge of (+1.049 ± 0.002)*e* compared to +1.061*e* in the reactant BiI_3 and are, therefore, in a reduced state in $MA_3Bi_2I_9$ as compared to BiI_3. This reduction of the Bi cation is also supported by the shift in experimental XPS peak towards lower binding energy as shown in **Figure 6c**. On comparing the average Bader charge of I anions in the primary reactants, i.e. the weighted average of the Bader charge of I in MAI and BiI_3 (–0.459*e*) to that in $MA_3Bi_2I_9$ (–0.472*e*), we find that the I anions are also reduced. This gain of electrons is also confirmed by the shift of the XPS peak for I anion towards lower binding energy as shown in **Figure 6d**. Moreover, the reduction of Bi and I ions in $MA_3Bi_2I_9$ with respect to the reactants (MAI and BiI_3) is accompanied by a simultaneous oxidation of the MA cations in $MA_3Bi_2I_9$ with respect to MAI, which balances out the net charge transfer. The net reduction of Bi and I requires a total charge transfer of 0.141*e* per formula unit of $MA_3Bi_2I_9$ to Bi and I (0.024*e* for Bi and 0.117*e* for I). This charge transfer is achieved by a transfer of electrons from MA cations to Bi and I as the reaction proceeds. The net average charge on MA cation is (+0.668*e*) and (+0.715*e*) in MAI and $MA_3Bi_2I_9$ respectively, which amounts to a net charge transfer of 0.141*e* per formula unit of $MA_3Bi_2I_9$ from MA to Bi and I.

View Article Online
DOI: 10.1039/C7TA06578G

Finally, the charge transfer in H can be categorized into two types, based on the position of H in the MA cations. H atoms directly bonded to C and those directly bonded to N lead to two different bonding environments. The H atoms bonded to N show an atomic charge of +1 for both $MA_3Bi_2I_9$ and MAI. Whereas, the H atoms bonded to C show an average atomic charge of +0.081 and +0.084 in $MA_3Bi_2I_9$ and MAI respectively. This difference in the atomic charge is due to the higher electronegativity of N than C, which renders the H-N bonds more ionic than the H–C bonds.

3.2 Optical characterization

Figure 7a shows the UV-vis absorption spectra of the 360 minute (2x) $MA_3Bi_2I_9$ film at wavelengths between 400 nm and 800 nm. The absorption onset of $MA_3Bi_2I_9$ was observed at approximately 600 nm. The presence of a peak at 511 nm before the onset of continuous absorption is attributed to excitons.[42, 44, 47, 48] We have verified separately the MAI and BiI_3 absorption spectra do not contain an exciton peak. This exciton peak has also been observed for single crystals of $MA_3Bi_2I_9$ from temperatures between 78 K to 301 K, and it starts to broaden as the temperature increases.[47] The thickness dependence of the exciton levels is shown **supporting information S5** where a stronger and narrower exciton peak is observed for a thinner film (~ 480 nm) whereas, a broader exciton peak is observed for a thicker (~ 1000 nm) film.

The bandgap of $MA_3Bi_2I_9$ films was calculated first by establishing a baseline and removing the exciton peak from the absorption spectrum. Then by plotting the baseline as a Tauć plot and using the equation[49]:

$$\alpha h\upsilon = \beta(h\upsilon - E_g)^n \qquad [2]$$

where α is the absorption coefficient, $h\upsilon$ is the photon energy, β is a constant, and E_g is the bandgap; a linear fit is used to extract the bandgap. Assuming the lowest energy optical transition

View Article Online
DOI: 10.1039/C7TA06578G

in $MA_3Bi_2I_9$ is indirect (see DFT calculations below), n=1/2 is used in the evaluation. The inset of **Figure 7a** shows the Tauć plot, and the extrapolated bandgap is 1.80 eV. The value of the $MA_3Bi_2I_9$ bandgap is in line with those reported by Lyu et al.[20]

Figure 7b shows the electronic band structure of $MA_3Bi_2I_9$ calculated using PBEsol with spin-orbit coupling (SOC) along the high symmetry points in the Brillouin zone. Using the PBEsol functional and SOC effects, we find $MA_3Bi_2I_9$ has an indirect band gap of 1.77 eV from K (1/3, 1/3, 0) in the valence band to (0.05, 0.05, 0) in the conduction band as shown in Figure **7b**. The calculated direct band gap is 1.89 eV and occurs at (0.075, 0.075, 0). The indirect and direct transitions are shown as red and black arrows respectively in Figure **7b.** $MA_3Bi_2I_9$ exhibits relatively flat bands as compared to the more promising organohalide perovskite solar cell absorbers such as $CH_3NH_3PbI_3$, [50, 51] which is typical for $A_3Bi_2I_9$ compounds[17] because of the disrupted octahedra-connectivity along all three crystallographic directions.

We also calculated the band structure using the hybrid Heyd-Scuseria-Ernzerhof (HSE06) functional with SOC effects,[52] which is known to result in better band gap estimation for a variety of semiconductors, as shown in **supporting information S6**. We find HSE06 overestimates the bandgap with an indirect band gap of 2.41 eV from K (1/3, 1/3, 0) in the valence band to (0.05, 0.05, 0) in the conduction band, and a direct band gap of 2.53 eV at K (1/3, 1/3, 0). Both the indirect and direct transitions are shown as red and black arrows respectively in the **Figure S6**.

To extract the experimental band edge positions of the $MA_3Bi_2I_9$, CV measurements are shown in **Figure 7c**. $MA_3Bi_2I_9$ has the reduction peak edge at, E_{red} = -1.22 V. Referring to equation [1], the $MA_3Bi_2I_9$ conduction band edge position is therefore calculated as, E_{CB} = -3.505 eV with respect to vacuum. Using the bandgap obtained from UV-vis (1.80 eV), the valence

View Article Online
DOI: 10.1039/C7TA06578G

band edge position is calculated as E_{VB}= -5.30 eV. The data from UV-vis + CV measurements and DFT calculations are summarized in **Figure 7d**.

3.3 Electrical characterization

For the $MA_3Bi_2I_9$ film deposited twice (360 minute (2x)) on the quartz substrate, conductivity was measured using a van der Pauw four-point configuration. The conductivity is 9.7 $S \cdot cm^{-1}$ (i.e., resistivity 0.103 Ω·cm) at room temperature for a film with a thickness of 775 nm (see **supporting information S7** for thickness measurement using cross-section SEM image). The detailed result is shown in **Table 4** along with comparison of electrical data from other reports.[15,44] This conductivity is 1168x better than the reported conductivity (0.0083 $S \cdot cm^{-1}$) of a solution-processed,[20] 500 nm $MA_3Bi_2I_9$ film highlighting the importance of the type of synthesis in determining film properties.

Room temperature Hall measurement was performed to determine conductivity type, carrier mobility and concentration of the $MA_3Bi_2I_9$ film. According to the measurements, the Hall coefficient is negative, which indicates the carriers to be *n*-type for the CVD $MA_3Bi_2I_9$ film. This result is in contrast to the solution processed $MA_3Bi_2I_9$ film which shows *p*-type conductivity.[20, 53] Further, the calculated carrier concentration of the CVD $MA_3Bi_2I_9$ film is 3.36 x 10^{18} cm^{-3}, which is 2 orders higher in magnitude than solution-based, undoped $MA_3Bi_2I_9$ films.[20, 53] Finally, the mobility was estimated to be 18 $cm^2/V.s$. This is higher compared to the mobility reported by Lyu et al.,[20] of 1 $cm^2/V.s$ and Vigneshwaran et al.,[53] of 2.28 $cm^2/V.s$. The improved carrier concentration and mobility highlight typical advantages that vapor phase processing of $MA_3Bi_2I_9$ films have over solution-based techniques including, minimal impurities, better crystallinity and film morphology.

View Article Online
DOI: 10.1039/C7TA06578G

3.4 Film stability

It has been reported that the $MA_3Bi_2I_9$ is stable in ambient, thus presenting a significant advantage over other organic halide perovskite candidates.[54] However, in our work we find that $MA_3Bi_2I_9$ film exposed to ambient (room temperature, 45% humidity and 1 atm) undergoes changes to its composition and degradation to its optical and electrical properties. In **Figure 8a**, a loss of N is detected in the $MA_3Bi_2I_9$ film exposed to the ambient in just 5 days. The absence of N has been observed by Li et al.,[55] for degraded Pb-based perovskite films as well. Further, in **supporting information S8**, we provide the XPS 1s fine spectra of O and 4f fine spectra of Bi in the $MA_3Bi_2I_9$ film. The O 1s shows the characteristic O peak associated with surface adsorbed hydroxyl groups with an additional shoulder corresponding to Bi-O bond formation after 5 days and growing stronger after 14 days of exposure to the ambient. Similarly, the Bi 4f shows signs of oxidation as well after 5 days. **Figure 8b** shows XPS fine spectra of I $3d_{7/2}$ and $3d_{5/2}$ for fresh films and for films exposed 5 and 14 days to the ambient. Unlike N and O, there is no noticeable change observed to the I 3d fine spectra after 5 days. However, shoulders appear for the I $3d_{7/2}$ and $3d_{5/2}$ peaks on the higher binding energy side after 14 days, indicating oxidation[56] of I. Thus, from XPS data it can be concluded that, while the loss of surface N and oxygen incorporation (most likely associated with Bi) is a rapid process, iodine oxidation is a slower process.

The compositional changes in the $MA_3Bi_2I_9$ are accompanied by changes to optical and electrical properties. **Figure 8c** shows the UV-vis absorption spectra of the $MA_3Bi_2I_9$ film exposed to ambient over a period of 5 days. The characteristic 510 nm exciton peak disappears on day 5. Correspondingly, the insets in **Figure 8c** show the film changes color from bright orange to a pale shade of yellow. In **Figure 8d**, the excitonic intensity at 510 nm (black, left axis) and the 4-wire resistivity (red, right axis) are plotted as a function of time over a five day

View Article Online
DOI: 10.1039/C7TA06578G

period. A bi-exponential model involving two time constants is used to fit the increase in resistivity over time. Two time constants, $\tau_1 = 0.1$ day and τ_2 = 1.7 days are obtained with a model fit that has an adjusted $r^2 \sim 0.99$.

The XPS analysis along with the bi-exponential decay of resistance suggests two decay mechanisms might be operative in degrading the $MA_3Bi_2I_9$ films. First, the time constant $\tau_1 = 0.1$ day could indicate surface oxidation of $MA_3Bi_2I_9$ where the Bi may be oxidized to Bi_2O_3. In line with this assumption, it can be seen that the exciton peak intensity only slightly degrades in the initial period. This is because the surface Bi_2O_3 layer may provide temporary protection[24] from further attack by ambient O_2, keeping the excitonic modes active in the bulk. On the other hand τ_2 = 1.7 days indicates the slower diffusion-limited oxidation of the bulk $MA_3Bi_2I_9$, and as the film gets oxidized after day 4, the exciton peak intensity rapidly degrades.

4 Conclusions

In conclusion, we have demonstrated an atmospheric pressure chemical vapor deposition process for the deposition of $MA_3Bi_2I_9$ perovskite film. The film is deposited using co-sublimation of methylammonium iodide (kept at 199 ^oC) and BiI_3 (kept at 230 ^oC) as precursors in a flow of inert Argon. The temperature of deposition is 160 ^oC. The key advantages of this synthesis approach is that the deposition is at atmospheric pressure and at low temperatures, which opens the possibility for depositing $MA_3Bi_2I_9$ films in high volume, cleanroom compatible, manufacturing environments. The deposition on flexible Willow® glass has been demonstrated.

Well-developed crystals are obtained after 360 minutes of deposition. Repeating the process twice leads to dense, high quality polycrystalline films. Optical bandgap is measured to be 1.80 eV. Room temperature Hall measurements on 775 nm thick $MA_3Bi_2I_9$ films indicate

View Article Online
DOI: 10.1039/C7TA06578G

them to be *n*-type with a carrier concentration of 3.36 x 10^{18} cm^{-3} and a Hall mobility of 18 $cm^2/V.s$; values superior to solution processed, undoped films. The $MA_3Bi_2I_9$ films oxidize under ambient conditions in a matter of ~ 5 days and in the process, 1) N is lost, 2) excitonic peaks are quenched and, 3) resistivity increases with a bi-exponential decay with time constants related to a fast surface oxidation mechanism, followed by a slower oxidation of the bulk film.

5 Acknowledgements

Partial support for this work was provided under the U.S.-India Partnership to Advance Clean Energy-Research (PACE-R) for the Solar Energy Research Institute for India and the United States (SERIIUS), funded jointly by the U.S. Department of Energy (Office of Science, Office of Basic Energy Sciences, and Energy Efficiency and Renewable Energy, Solar Energy Technology Program, under subcontract DE-AC36-08GO28308 to the national Renewable Energy Laboratory, Golden, Colorado) and the Government of India, through the Department of Science and Technology under Subcontract IUSSTF/JCERDC-SERIIUS/2012 is acknowledged. Willow® glass substrates were kindly provided by Dr. Sean Garner from Corning. Partial support from U.S. Army RDECOM Acquisition Grant W911NF-15-1-0178, Subgrant RSC15032 is acknowledged. R.M. acknowledges support from Oak Ridge Associated Universities through a Ralph E. Powe Junior Faculty Enhancement award. The XPS measurements were made possible through the support from NSF MRI Grant 1337374. The microscopy facility and support from Dr. Huafang Li at the Institute of Materials Science and Engineering are acknowledged. The authors thank R. A. Loomis for use of his spectrometer and integrating sphere. Help from Dr. D.C. Osborn at the XRD Facilities at University of Missouri St. Louis is acknowledged. This work used computational resources of the Extreme Science and Engineering Discovery

View Article Online
DOI: 10.1039/C7TA06578G

Environment (XSEDE), which is supported by National Science Foundation grant number ACI-1053575.

View Article Online
DOI: 10.1039/C7TA06578G

References:

1. A. Kojima, K. Teshima, Y. Shirai and T. Miyasaka, *J. Am. Chem. Soc.*, 2009, **131**, 6050-6051.
2. NREL, Best Research-Cell Efficiencies, https://www.nrel.gov/pv/assets/images/efficiency-chart.png).
3. C. Wehrenfennig, G. E. Eperon, M. B. Johnston, H. J. Snaith and L. M. Herz, *Adv. Mater.*, 2014, **26**, 1584-1589.
4. J.-H. Im, C.-R. Lee, J.-W. Lee, S.-W. Park and N.-G. Park, *Nanoscale*, 2011, **3**, 4088-4093.
5. J. H. Noh, S. H. Im, J. H. Heo, T. N. Mandal and S. I. Seok, *Nano Lett.*, 2013, **13**, 1764-1769.
6. S. D. Stranks, G. E. Eperon, G. Grancini, C. Menelaou, M. J. Alcocer, T. Leijtens, L. M. Herz, A. Petrozza and H. J. Snaith, *Science*, 2013, **342**, 341-344.
7. G. Xing, N. Mathews, S. Sun, S. S. Lim, Y. M. Lam, M. Grätzel, S. Mhaisalkar and T. C. Sum, *Science*, 2013, **342**, 344-347.
8. S. F. Hoefler, G. Trimmel and T. Rath, *Monatsh. Chem.*, 2017, **148**, 795-826.
9. B. Hailegnaw, S. Kirmayer, E. Edri, G. Hodes and D. Cahen, *The journal of physical chemistry letters*, 2015, **6**, 1543-1547.
10. G. Nagabhushana, R. Shivaramaiah and A. Navrotsky, *Proceedings of the National Academy of Sciences*, 2016, **113**, 7717-7721.
11. A. Babayigit, A. Ethirajan, M. Muller and B. Conings, *Nat. Mater.*, 2016, **15**, 247-251.
12. M. Saliba, T. Matsui, J.-Y. Seo, K. Domanski, J.-P. Correa-Baena, M. K. Nazeeruddin, S. M. Zakeeruddin, W. Tress, A. Abate and A. Hagfeldt, *Energy Environ. Sci.*, 2016, **9**, 1989-1997.
13. Y. Zhou, Z. Zhou, M. Chen, Y. Zong, J. Huang, S. Pang and N. P. Padture, *J. Mater. Chem. A*, 2016, **4**, 17623-17635.
14. N. Rajamanickam, S. Kumari, V. K. Vendra, B. W. Lavery, J. Spurgeon, T. Druffel and M. K. Sunkara, *Nanotechnology*, 2016, **27**, 235404.
15. B. W. Park, B. Philippe, X. Zhang, H. Rensmo, G. Boschloo and E. M. Johansson, *Adv. Mater.*, 2015, **27**, 6806-6813.

View Article Online
DOI: 10.1039/C7TA06578G

16. A. J. Lehner, D. H. Fabini, H. A. Evans, C.-A. Hébert, S. R. Smock, J. Hu, H. Wang, J. W. Zwanziger, M. L. Chabinyc and R. Seshadri, *Chem. Mater.*, 2015, **27**, 7137-7148.
17. X. Huang, S. Huang, P. Biswas and R. Mishra, *J. Phys. Chem. C*, 2016, **120**, 28924-28932.
18. A. Kulkarni, T. Singh, M. Ikegami and T. Miyasaka, *RSC Adv.*, 2017, **7**, 9456-9460.
19. C. T. Zuo and L. M. Ding, *Angewandte Chemie-International Edition*, 2017, **56**, 6528-6532.
20. M. Lyu, J.-H. Yun, M. Cai, Y. Jiao, P. V. Bernhardt, M. Zhang, Q. Wang, A. Du, H. Wang, G. Liu and L. Wang, *Nano Res.*, 2016, **9**, 692-702.
21. A. M. Ganose, C. N. Savory and D. O. Scanlon, *Chem Commun (Camb)*, 2016, **53**, 20-44.
22. R. E. Brandt, V. Stevanović, D. S. Ginley and T. Buonassisi, *Mrs Communications*, 2015, **5**, 265-275.
23. K. Eckhardt, V. Bon, J. Getzschmann, J. Grothe, F. M. Wisser and S. Kaskel, *Chem. Commun.*, 2016, **52**, 3058-3060.
24. R. L. Hoye, R. E. Brandt, A. Osherov, V. Stevanović, S. D. Stranks, M. W. Wilson, H. Kim, A. J. Akey, J. D. Perkins and R. C. Kurchin, *Chem. Eur. J.*, 2016, **22**, 2605-2610.
25. T. Okano and Y. Suzuki, *Mater. Lett.*, 2017, **191**, 77-79.
26. Z. Xiao, W. Meng, J. Wang, D. B. Mitzi and Y. Yan, *Materials Horizons*, 2017, **4**, 206-216.
27. M. Liu, M. B. Johnston and H. J. Snaith, *Nature*, 2013, **501**, 395-398.
28. Y. X. Zhao and K. Zhu, *J. Phys. Chem. Lett.*, 2014, **5**, 4175-4186.
29. M. M. Tavakoli, L. L. Gu, Y. Gao, C. Reckmeier, J. He, A. L. Rogach, Y. Yao and Z. Y. Fan, *Scientific Reports*, 2015, **5**.
30. A. Cuña, I. Aguiar, A. Gancharov, M. Pérez and L. Fornaro, *Cryst. Res. Technol.*, 2004, **39**, 899-905.
31. A. Dualeh, P. Gao, S. I. Seok, M. K. Nazeeruddin and M. Grätzel, *Chem. Mater.*, 2014, **26**, 6160-6164.
32. D. V. Ragone, *Thermodynamics of materials - I*, Wiley, New York, 1995.
33. G. Kresse and J. Furthmuller, *Phys. Rev. B*, 1996, **54**, 11169-11186.

View Article Online
DOI: 10.1039/C7TA06578G

34. J. P. Perdew, A. Ruzsinszky, G. I. Csonka, O. A. Vydrov, G. E. Scuseria, L. A. Constantin, X. Zhou and K. Burke, *Phys Rev Lett*, 2008, **100**, 136406.
35. P. E. Blöchl, *Phys. Rev. B*, 1994, **50**, 17953.
36. H. J. Monkhorst and J. D. Pack, *Phys. Rev. B*, 1976, **13**, 5188-5192.
37. G. Henkelman, A. Arnaldsson and H. Jónsson, *Comput. Mater. Sci.*, 2006, **36**, 354-360.
38. E. Sanville, S. D. Kenny, R. Smith and G. Henkelman, *J. Comput. Chem.*, 2007, **28**, 899-908.
39. W. Tang, E. Sanville and G. Henkelman, *J. Phys. Condens. Matter*, 2009, **21**, 084204.
40. D. Nason and L. Keller, *J. Cryst. Growth*, 1995, **156**, 221-226.
41. K. M. Boopathi, S. Raman, R. Mohanraman, F.-C. Chou, Y.-Y. Chen, C.-H. Lee, F.-C. Chang and C.-W. Chu, *Sol. Energy Mater. Sol. Cells*, 2014, **121**, 35-41.
42. M. Abulikemu, S. Ould-Chikh, X. Miao, E. Alarousu, B. Murali, G. O. N. Ndjawa, J. Barbé, A. El Labban, A. Amassian and S. Del Gobbo, *J. Mater. Chem. A*, 2016, **4**, 12504-12515.
43. M. E. Kamminga, A. Stroppa, S. Picozzi, M. Chislov, I. A. Zvereva, J. Baas, A. Meetsma, G. R. Blake and T. T. Palstra, *Inorg Chem*, 2017, **56**, 33-41.
44. M. Scholz, O. Flender, K. Oum and T. Lenzer, *J. Phys. Chem. C*, 2017, **121**, 12110-12116.
45. C. Ran, Z. Wu, J. Xi, F. Yuan, H. Dong, T. Lei, X. He and X. Hou, *J Phys Chem Lett*, 2017, **8**, 394-400.
46. L. Liu, J. A. McLeod, R. Wang, P. Shen and S. Duhm, *Appl. Phys. Lett.*, 2015, **107**, 061904.
47. T. Kawai, A. Ishii, T. Kitamura, S. Shimanuki, M. Iwata and Y. Ishibashi, *J. Phys. Soc. Jpn.*, 1996, **65**, 1464-1468.
48. S. Öz, J.-C. Hebig, E. Jung, T. Singh, A. Lepcha, S. Olthof, F. Jan, Y. Gao, R. German, P. H. M. van Loosdrecht, K. Meerholz, T. Kirchartz and S. Mathur, *Sol. Energy Mater. Sol. Cells*, 2016, **158**, 195-201.
49. J. I. Pankove, *Optical processes in semiconductors*, Courier Corporation, 2012.
50. P. Umari, E. Mosconi and F. De Angelis, *Scientific Reports*, 2014, **4**, 4467.
51. A. S. Thind, X. Huang, J. Sun and R. Mishra, *Chem. Mater.*, 2017, DOI: 10.1021/acs.chemmater.7b01781.

View Article Online
DOI: 10.1039/C7TA06578G

52. J. Heyd, G. E. Scuseria and M. Ernzerhof, *J. Chem. Phys.*, 2003, **118**, 8207-8215.
53. M. Vigneshwaran, T. Ohta, S. Iikubo, G. Kapil, T. S. Ripolles, Y. Ogomi, T. Ma, S. S. Pandey, Q. Shen and T. Toyoda, *Chem. Mater.*, 2016, **28**, 6436-6440.
54. R. L. Hoye, R. E. Brandt, A. Osherov, V. Stevanović, S. D. Stranks, M. W. Wilson, H. Kim, A. J. Akey, J. D. Perkins and R. C. Kurchin, *Chemistry–A European Journal*, 2016.
55. Y. Li, X. Xu, C. Wang, C. Wang, F. Xie, J. Yang and Y. Gao, 2015.
56. J. Chastain, R. C. King and J. Moulder, *Handbook of X-ray photoelectron spectroscopy: a reference book of standard spectra for identification and interpretation of XPS data*, Physical Electronics Division, Perkin-Elmer Corporation Eden Prairie, Minnesota, 1992.

View Article Online
DOI: 10.1039/C7TA06578G

List of Figures

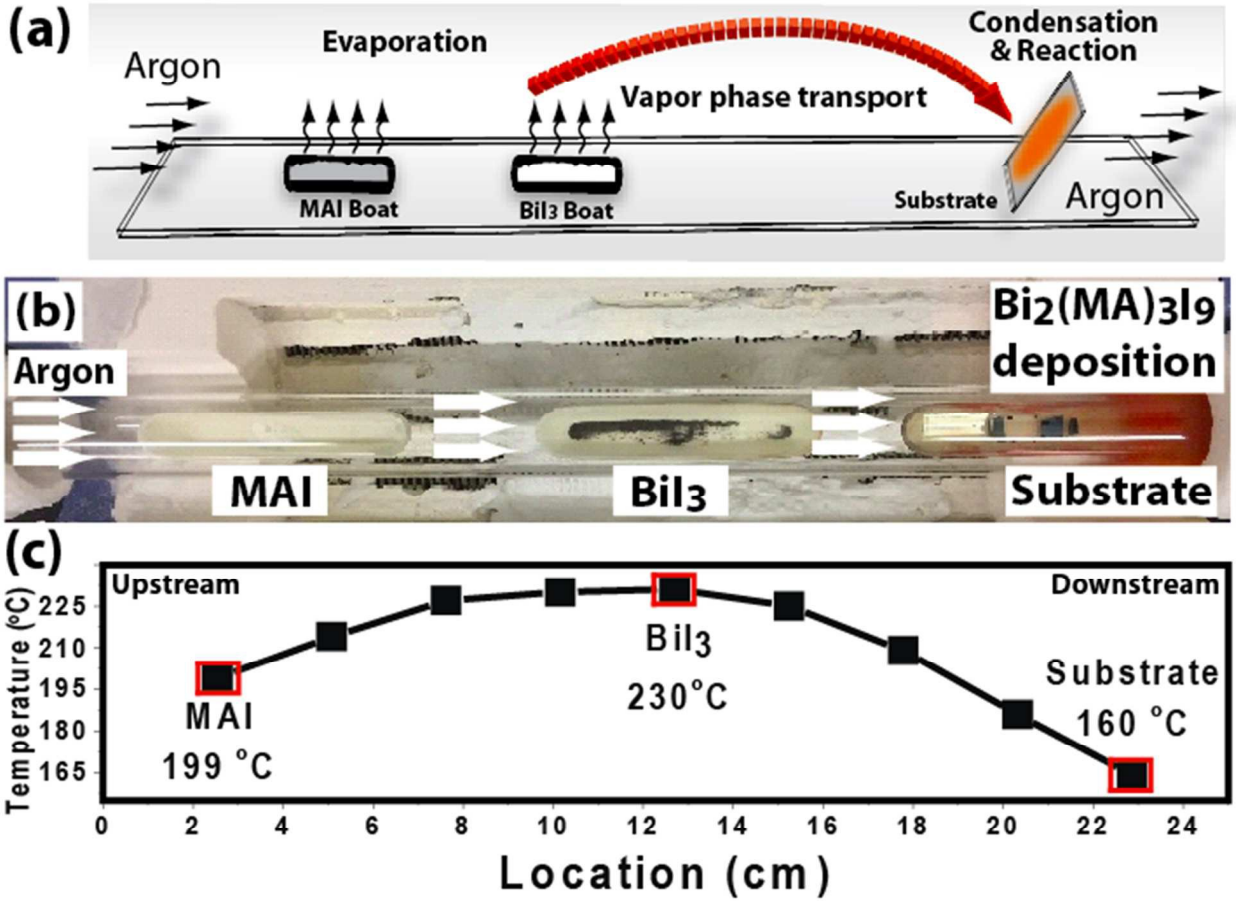

Figure 1: (a) Schematic of APCVD for $MA_3Bi_2I_9$ thin films, (b) Image of MAI and BiI_3 boats inside the tube furnace and (c), temperature profile of the tube furnace showing the MAI and BiI_3 sublimation temperatures and $MA_3Bi_2I_9$ film deposition temperature.

View Article Online
DOI: 10.1039/C7TA06578G

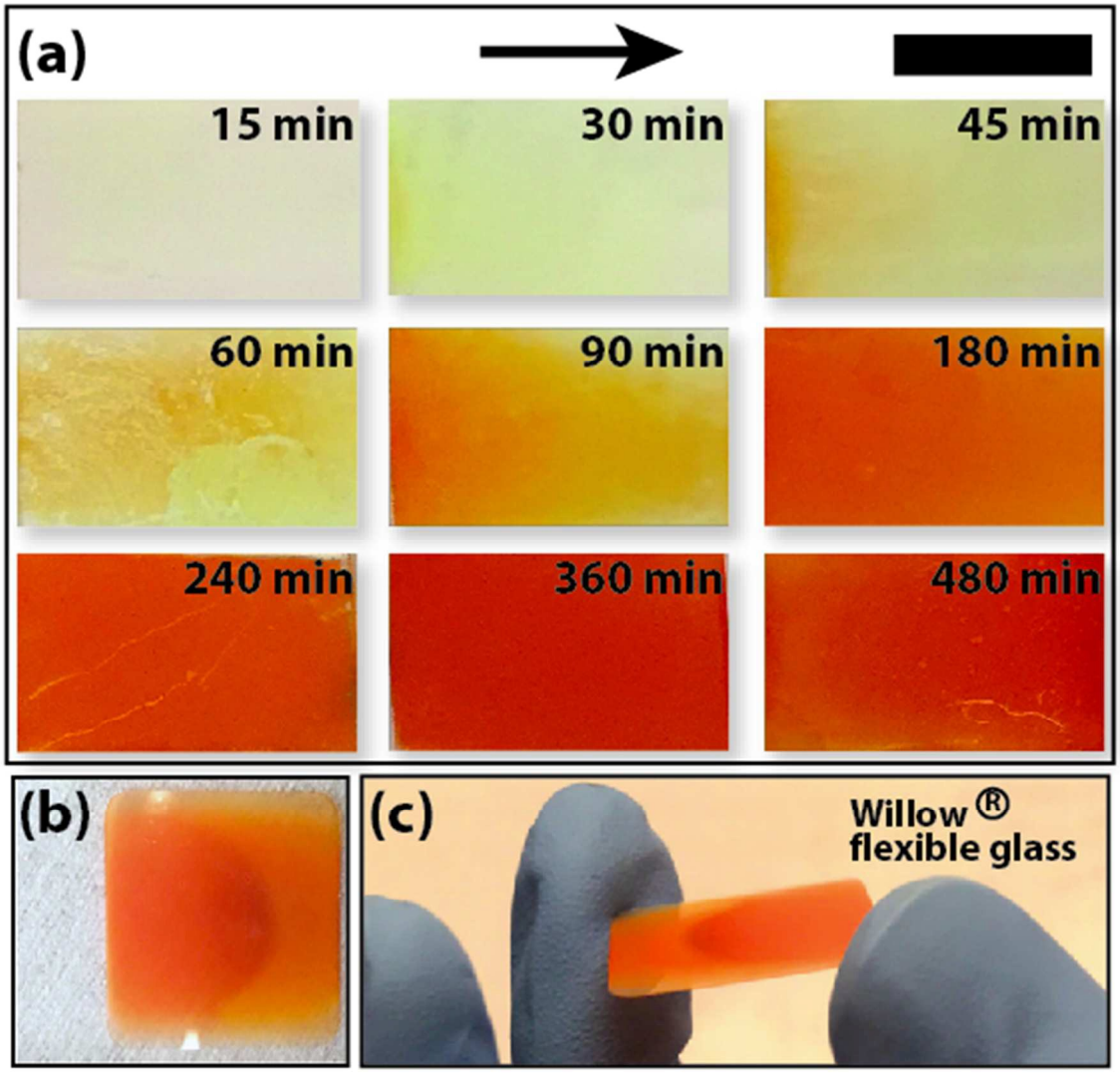

Figure 2: (a) Optical images of APCVD $MA_3Bi_2I_9$ films on glass substrate for varying times of deposition. Arrow represents direction of Ar flow in the furnace. Scale bar = 1 cm. (b) $MA_3Bi_2I_9$ deposited for 360 minutes on Willow® flexible glass of size 2 cm x 2cm and (c) substrate held in hand.

View Article Online
DOI: 10.1039/C7TA06578G

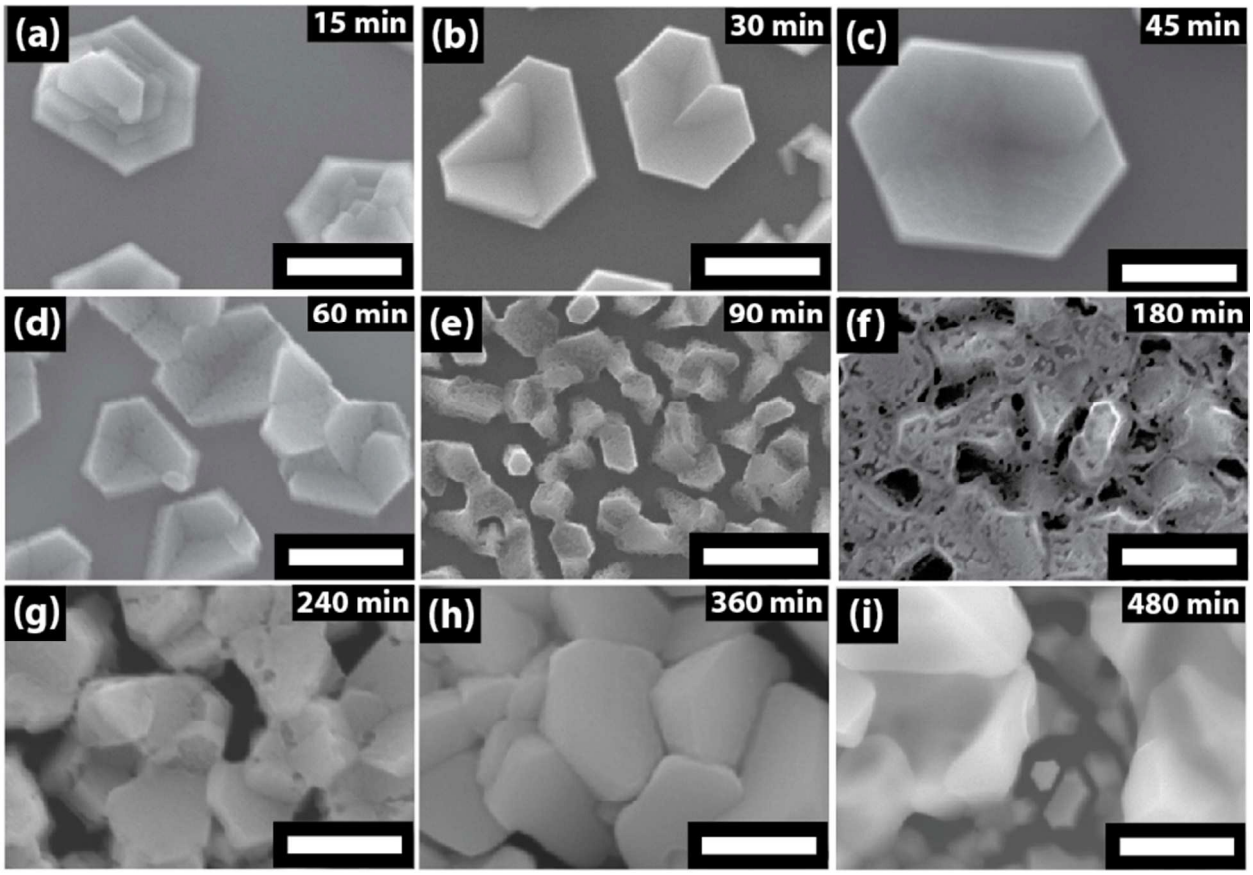

Figure 3: SEM images of APCVD films for varying times of deposition. Scale bar = 500 nm.

View Article Online
DOI: 10.1039/C7TA06578G

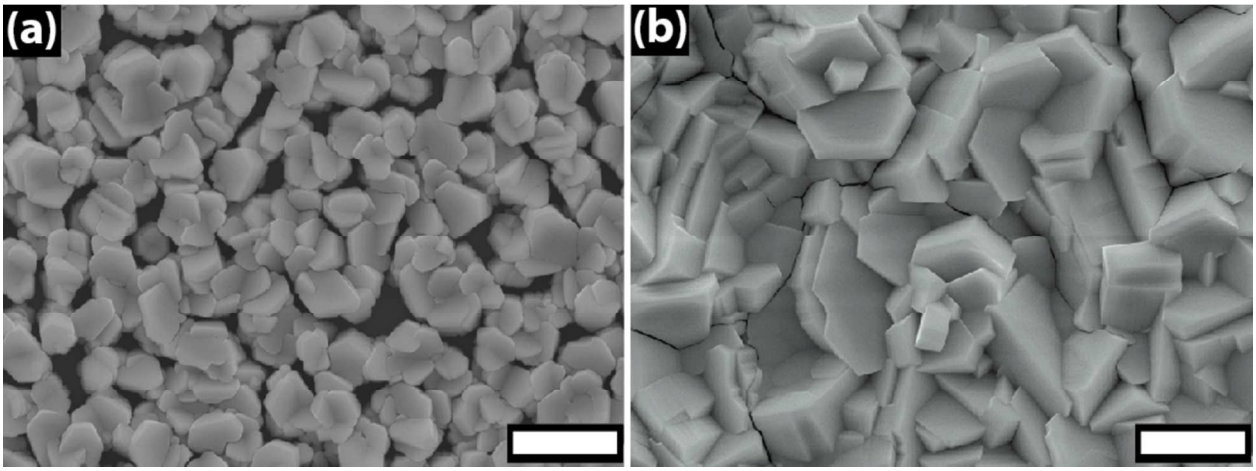

Figure 4: (a) Low magnification image of $MA_3Bi_2I_9$ film deposited for 360 minutes showing the intergranular gaps in the polycrystalline film. (b) A repeat of the same process (i.e., 360 minutes (2×)), eliminates these gaps and produces a dense, polycrystalline film. All optical and electrical measurements were performed on the 360 minutes (2×) sample. Scale bar = 2 μm.

View Article Online
DOI: 10.1039/C7TA06578G

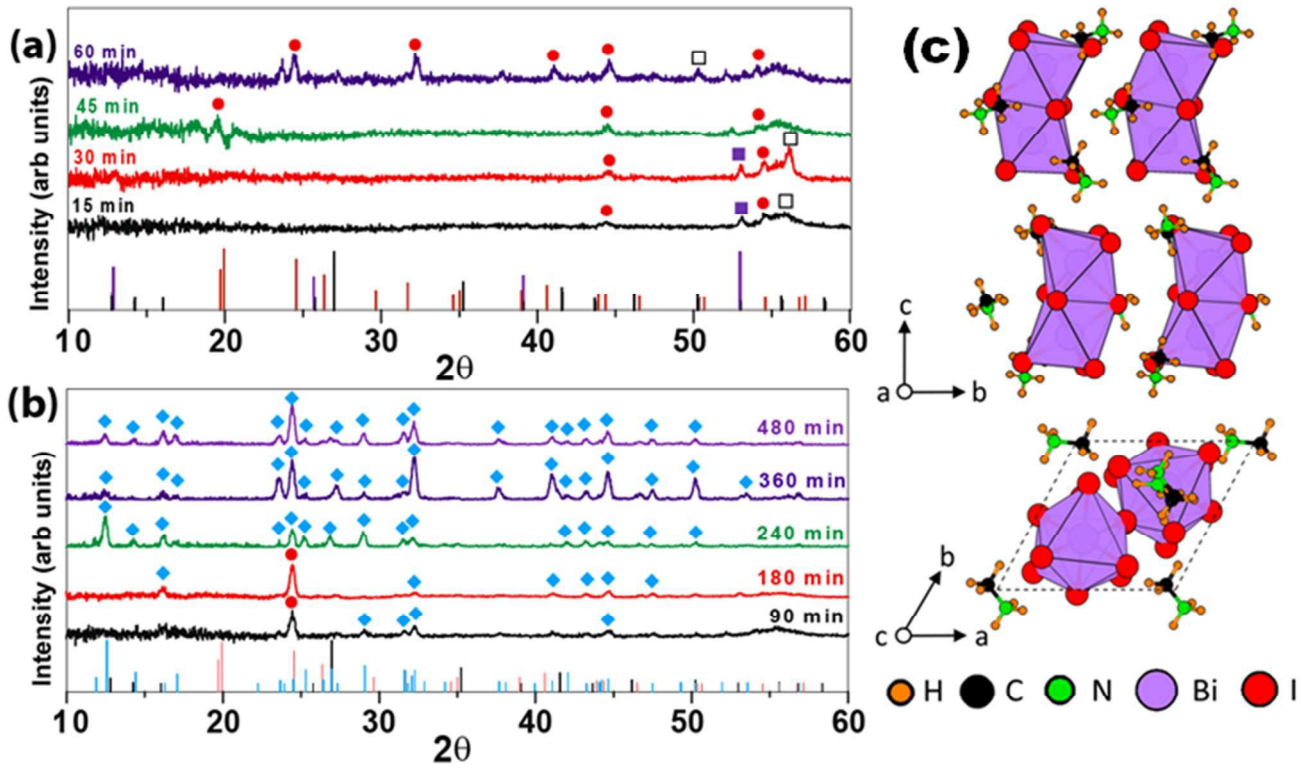

Figure 5 : XRD of films as a function of deposition time. For clarity, the XRD has been split into two graphs. (a) Variation of deposition time from 15 minutes to 60 minutes and (b) variation of deposition time from 90 minutes to 480 minutes. Single crystal BiI_3 reference is obtained from Boopathy et al., and is indexed with symbol '■' with violet staff. Polycrystalline BiI_3 is indexed as symbol '□' and black staff and obtained from JCPDS 48-1795. MAI reference is obtained from JCPDS 10-0737 and is indexed with symbol '●' and red staff. $MA_3Bi_2I_9$ reference is obtained from Abulikemu et al., and is indexed with symbol '♦' and cyan staff. (c) Crystal structure of $MA_3Bi_2I_9$ after relaxation along (100) (top) and (001) (bottom) crystallographic directions.

View Article Online
DOI: 10.1039/C7TA06578G

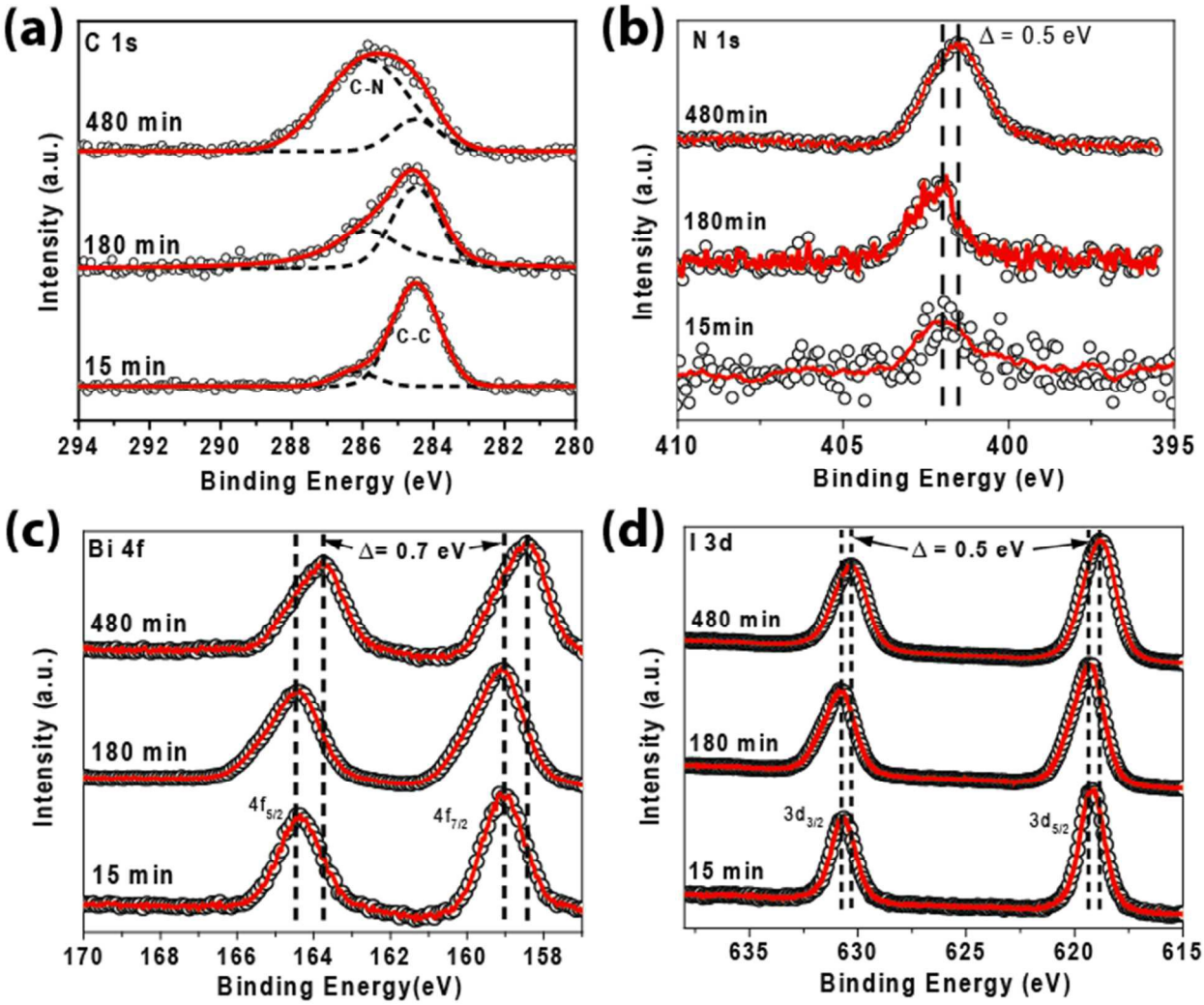

Figure 6: XPS fine spectra obtained from 15, 180 and 480 minute $MA_3Bi_2I_9$ thin films showing (a) Bi 4f, (b) I 3d, (c) N 1s and, (d) C 1s. The carbon 1s peak has been deconvoluted into two peaks related to adventitious carbon (284.5 eV) and C-N from the methylammonium group.

View Article Online
DOI: 10.1039/C7TA06578G

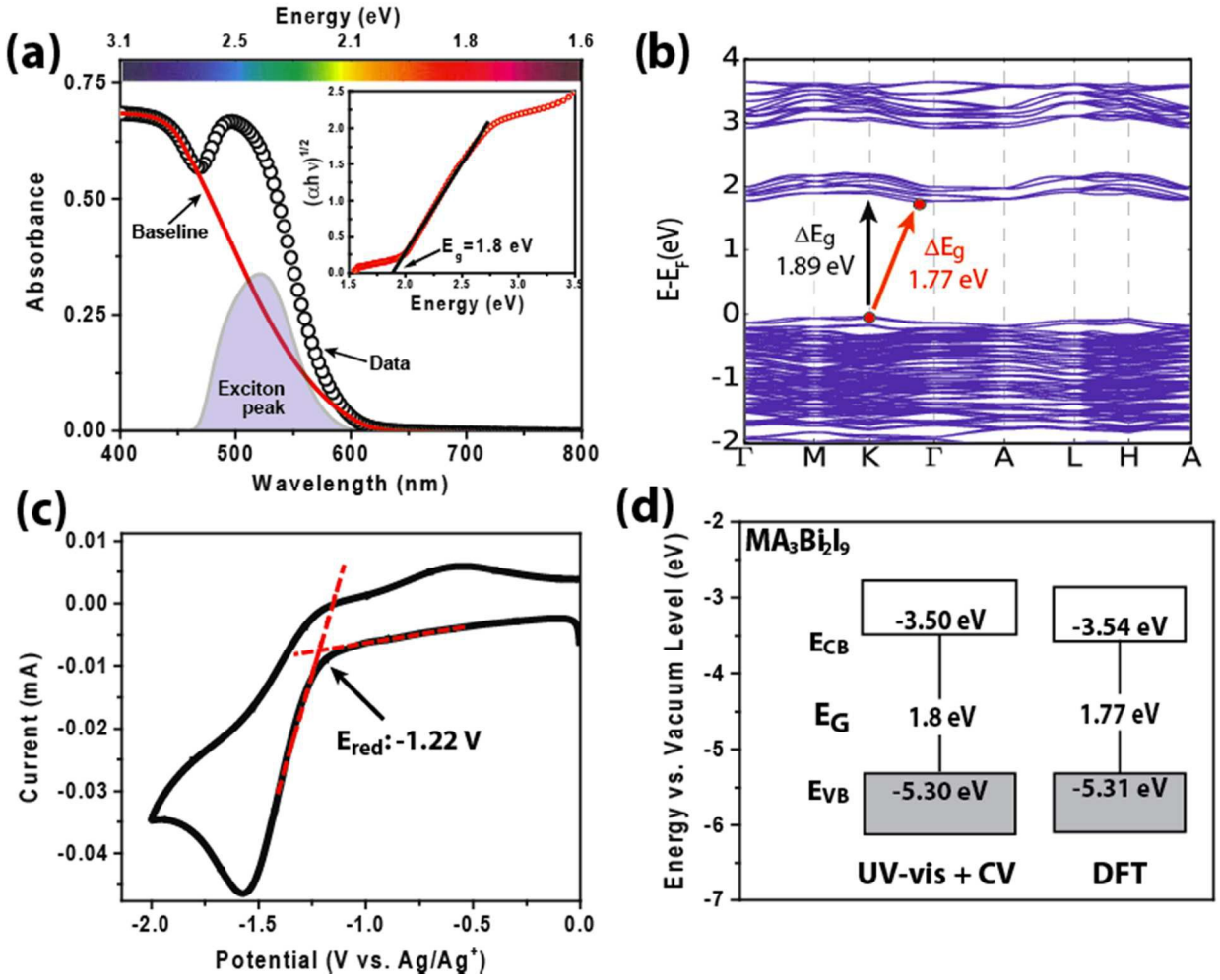

Figure 7: (a) UV- vis spectra of $MA_3Bi_2I_9$ film. Exciton peak is extracted and a Tauć plot of the baseline is used to measure the indirect bandgap 1.8 eV (b) DFT-calculated band structure for MA3Bi2I9 with calculated indirect bandgap of 1.77 eV (red arrow) and direct bandgap of 1.89 eV (black arrow) (c) Cyclic voltammetry curve (vs. Ag/Ag+ electrode) for $MA_3Bi_2I_9$ (d) Band edge information from experimental (UV-vis + CV) and DFT calculations.

View Article Online
DOI: 10.1039/C7TA06578G

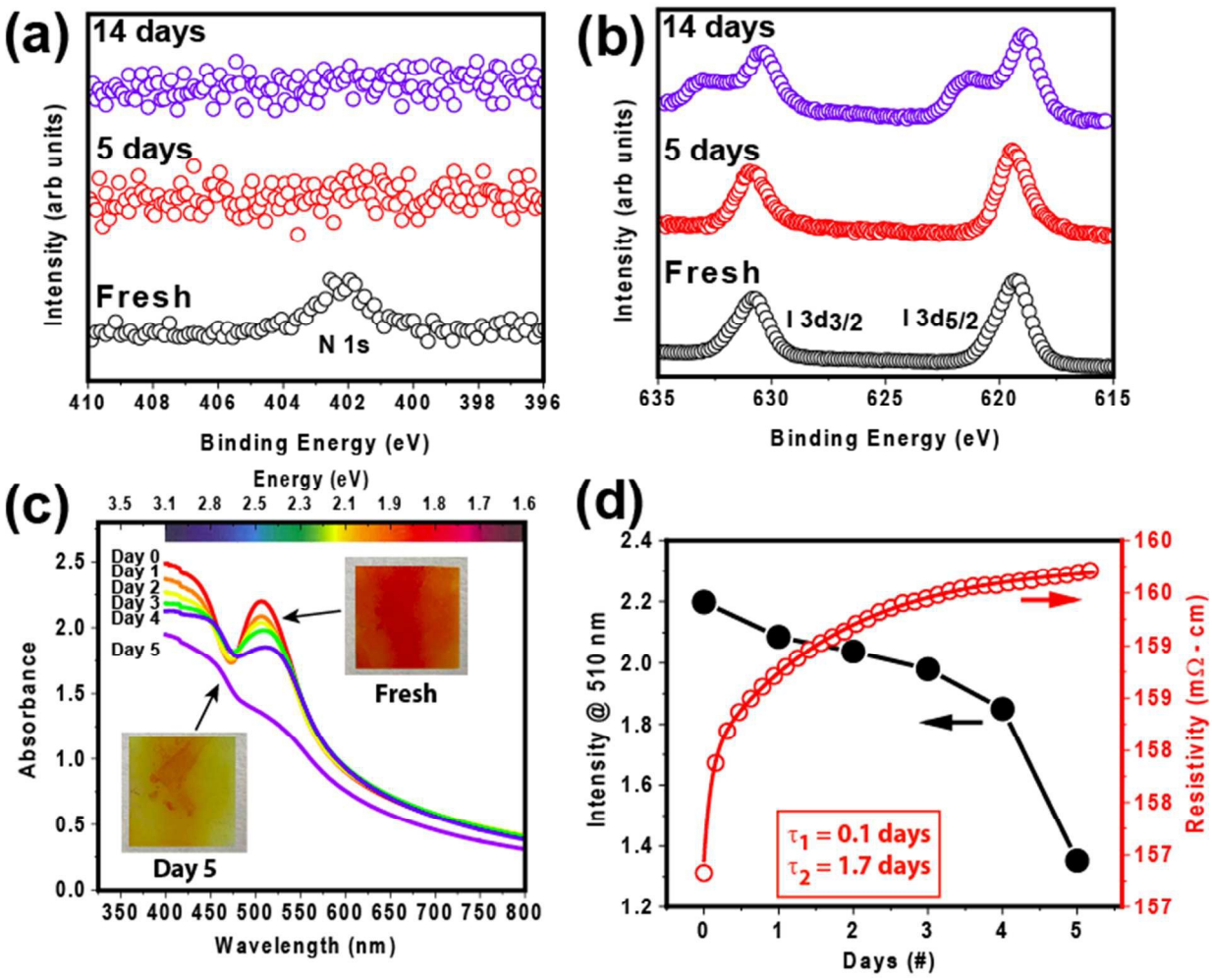

Figure 8: (a) XPS fine spectra of N 1s shows absence of N after just 5 days exposure in ambient. (b) XPS fine spectra of I 3d for fresh, after 5 (no change) and 14 days in ambient. The splitting of the 3d peaks after 14 days to higher binding energy indicates oxidation of the iodine. (c) UV-vis spectra from day 0 (fresh) to day 5 shows a gradual decay of the excitonic peak while insets show actual film fading color, and (d) Change in exciton peak intensity (black, left axis) and electrical resistivity (red, right axis) as a function of number of days exposed to ambient. The increase in resistivity follows a bi-exponential decay with time constants 0.1 and 1.7 days.

View Article Online
DOI: 10.1039/C7TA06578G

List of Tables

	Precursor compound	Process	Temperature (^{o}C)	Partial pressure	MAI: BiI_3 ratio	
					Sublimation	Deposition
1	MAI	Sublimation	199 ^{o}C	0.0846	4.7:1	
2	BiI_3	Sublimation	230 ^{o}C	0.0180		
3	MAI	Deposition	160 ^{o}C	0.01133		87:1
4	BiI_3	Deposition	160 ^{o}C	0.00013		

Table 1: The partial pressures obtained from thermogravimetric analysis of MAI and BiI_3 powders. MAI and BiI_3 vapor pressures were calculated at its sublimation temperatures of 199 ^{o}C and 230 ^{o}C, respectively. The ratio of MAI: BiI_3 vapor pressure is 4.7:1. Similarly, at the point of condensation where the temperature is 160 ^{o}C, the ratio of MAI: BiI_3 vapor pressures was 87:1, indicating a far higher driving force for BiI_3 to condense, nucleate and grow.

View Article Online
DOI: 10.1039/C7TA06578G

Sample	Binding Energy (eV)		
	N 1s	**Bi $4f_{7/2}$**	**I $3d_{5/2}$**
15 min	402.0	159.1	619.3
180 min	402.0	159.0	619.2
480 min	401.5	158.4	618.8

Table 2: XPS peak positions of N 1s, Bi $4f_{7/2}$ and I $3d_{5/2}$ in the $MA_3Bi_2I_9$ films deposited for 15, 180 and 480 minutes.

View Article Online
DOI: 10.1039/C7TA06578G

Element	$MA_3Bi_2I_9$	MAI	BiI_3
C	0.453 ± 0.015	0.445	
N	–2.982 ± 0.009	–3.029	
Bi	1.049 ± 0.002		1.061
I	–0.472 ± 0.009	–0.668	–0.354
H-1 (Bonded to C)	0.081 ± 0.013	0.084 ± 0.005	
H-2 (Bonded to N)	1	1	

Table 3: Calculated average Bader charges and their respective standard deviation (in units of *e*) for each elemental species in $MA_3Bi_2I_9$, MAI and BiI_3.

View Article Online
DOI: 10.1039/C7TA06578G

Synthesis process	**Thickness (nm)**	**Conductivity ($S \cdot cm^{-1}$)**	**Mobility ($cm^2/V \cdot s$)**	**Carrier density (cm^{-3})**
APCVD 360 minutes (2×) (this work)	775	9.7	18.0	*n*-type 3.36×10^{18}
Solution processed (Lyu et al.,[16])	500	0.0083	1.0	*p*-type 10^{16}
Solution processed, Sulphur doped (Vigneshwaran et al.,[46])	unknown	839	2.28	*p*-type 2.3×10^{21}

Table 4: Comparison of Hall measurement data of $MA_3Bi_2I_9$ films deposited using various synthesis techniques.

View Article Online
DOI: 10.1039/C7TA06578G

Table of contents

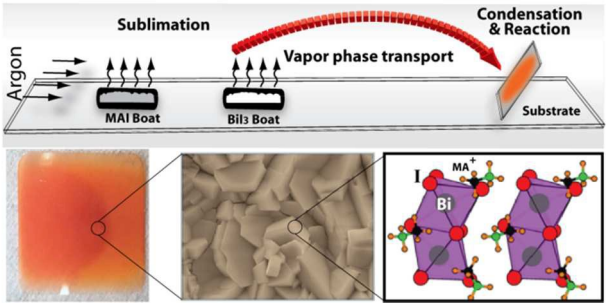

High quality methylammonium bismuth iodide films made using atmospheric chemical vapor deposition.